Journal Pre-proof

Inactivation of *Atp7b* copper transporter in intestinal epithelial cells is associated with altered lipid processing and cell growth machinery independent from hepatic copper accumulation and severity of liver histology

Amanda Caceres, Noreene M. Shibata, Christian D. Davalos-Gutierrez, Gaurav V. Sarode, Hisham Hussan, Margarida Bettencourt, Adriana Fontes, Hans Zischka, Svetlana Lutsenko, Marie C. Heffern, Valentina Medici

PII: S0002-9440(25)00379-7

DOI: https://doi.org/10.1016/j.ajpath.2025.09.015

Reference: AJPA 4382

To appear in: *The American Journal of Pathology*

Received Date: 17 June 2025

Revised Date: 25 August 2025

Accepted Date: 10 September 2025

Please cite this article as: Caceres A, Shibata NM, Davalos-Gutierrez CD, Sarode GV, Hussan H, Bettencourt M, Fontes A, Zischka H, Lutsenko S, Heffern MC, Medici V, Inactivation of *Atp7b* copper transporter in intestinal epithelial cells is associated with altered lipid processing and cell growth machinery independent from hepatic copper accumulation and severity of liver histology, *The American Journal of Pathology* (2025), doi: https://doi.org/10.1016/j.ajpath.2025.09.015.

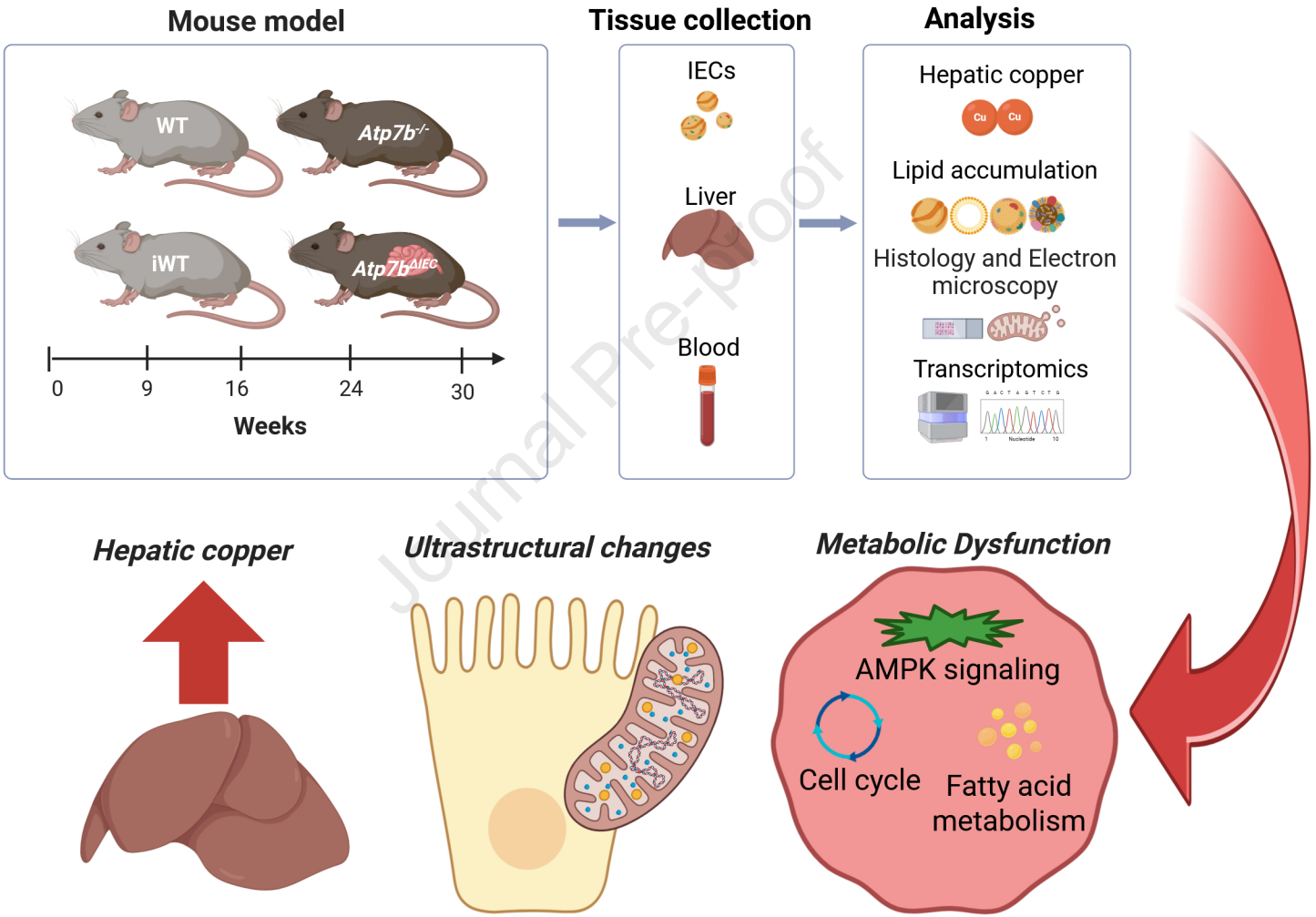

Inactivation of *Atp7b* copper transporter in intestinal epithelial cells is associated with altered lipid processing and cell growth machinery independent from hepatic copper accumulation and severity of liver histology

Amanda Caceres[1], Noreene M. Shibata[2], Christian D. Davalos-Gutierrez[1], Gaurav V. Sarode[2], Hisham Hussan[2], Margarida Bettencourt[2], Adriana Fontes[3], Hans Zischka[3], Svetlana Lutsenko[4], Marie C. Heffern[1], Valentina Medici[2]

1. Department of Chemistry, University of California Davis, CA, USA
2. Department of Internal Medicine, Division of Gastroenterology and Hepatology, University of California Davis, CA, USA
3. Institute of Molecular Toxicology and Pharmacology, Helmholtz Center Munich, German Research Center for Environmental Health, Neuherberg, Germany; Technical University Munich, Institute of Toxicology and Environmental Hygiene, Munich, Germany
4. Department of Physiology, Johns Hopkins Medical Institutes, Baltimore, MD, USA

Running Title: Role of the intestine in Wilson disease

Manuscript Information: pages=22; tables=2; figures=9

Sources of Support: UC Davis Division of Gastroenterology and Hepatology and UC Davis School of Medicine funds to V.M. The Hartwell Foundation, the UC Davis CAMPOS Program, NIH MIRA 5R35GM133684, P30DK11607, P30DK098722 and NSF CAREER 2048265 to M.C.H. ARCS Foundation Scholar Award to A.C.

Disclosures: No disclosures

Corresponding Author:

Valentina Medici M.D., F.A.A.S.L.D.

University of California, Davis

Department of Internal Medicine

Division of Gastroenterology and Hepatology

4150 V Street, Suite 3500

Sacramento, CA 95817

Office: 916-734-3751, Fax: 916-734-7908

Email: vmedici@ucdavis.edu

ABSTRACT

The clinical manifestations of Wilson disease (WD) are related to copper accumulation in the liver and brain, but little is known about the role of other organs expressing the ATP7B copper transporter on metabolic and ultrastructural changes characterizing WD. To examine the consequences of intestinal *Atp7b* inactivation in the absence of hepatic copper accumulation, a new mouse model (*Atp7b*$^{\Delta IEC}$) characterized by enterocyte-specific *Atp7b* inactivation was generated. *Atp7b*$^{\Delta IEC}$ mice were compared to wildtype mice with the same genetic background (iWT). The *Atp7b* global knockout (*Atp7b*$^{-/-}$) model of WD on a C57Bl/6 background was previously generated and compared to respective WT. Hepatic copper, lipid metabolism, liver and intestine histology and electron microscopy were assessed over time up to 30 weeks of age. Whereas there was no evidence of intestine copper accumulation in the *Atp7b*$^{\Delta IEC}$ mice, transcriptome analysis in *Atp7b*$^{\Delta IEC}$ mice revealed changes in genes involved in AMPK signaling, fatty acid metabolism, and cell cycle both with partial overlap between the intestinal epithelial cells and the liver. Mitochondrial and other ultrastructural changes were observed in the intestinal epithelial cells of both *Atp7b*$^{-/-}$ and *Atp7b*$^{\Delta IEC}$ mice. Intestine-specific *Atp7b* deficit affects systemic metabolic pathways and intestine morphology, and hepatic metabolic perturbations are associated with intestinal dysfunction, independently from hepatic copper accumulation, providing evidence that WD phenotype is at least partially influenced by organ-specific ATP7B variants.

INTRODUCTION

Copper metabolism and trafficking are highly regulated due to its essential role in multiple key metabolic pathways, and to avoid copper accumulation with ensuing, mitochondrial dysfunction, decreased glutathione levels, pro-mutagenic DNA adducts, and oxidative stress[1 2]. Copper is absorbed through the duodenum and proximal jejunum by the action of copper-specific transporter CTR1[3, 4]. The ATP7A transporter is localized in the basolateral membrane and is responsible for the release of copper in the portal circulation where copper is loosely bound to soluble chaperones, including albumin, histidines, and macroglobulines[5 6]. From the portal vein, copper reaches the liver where it is chaperoned into hepatocyte subcellular compartments, in particular mitochondria, trans Golgi network, and the nucleus. Ultimately, copper will be tightly bound to ceruloplasmin in a process facilitated by transmembrane copper transporter ATP7B. ATP7B is also responsible for excreting excess copper via the biliary tract. ATP7B is expressed in multiple organs, most importantly the liver and the brain, but it is also highly expressed in the intestinal epithelial cells (IECs) of the duodenum and jejunum[7]. ATP7B pathogenic variants and related transporter dysfunction are the cause of Wilson disease (WD), a rare autosomal recessive disease due to copper accumulation in the liver and in the brain. WD is a complex systemic metabolic disease where the clinical presentation is varied, often with unpredictable outcomes and response to treatment. The clinical presentation commonly includes hepatic steatosis[8, 9] as well as overlooked signs and symptoms derived from the gastrointestinal tract, including changes in bowel habits and abdominal pain[10, 11]. In addition, given the common hepatic and neurologic presentations, it is plausible the gut-liver-brain axis plays a role in the development of neuropsychiatric presentations. There is evidence of reduced and altered gut microbiota diversity in patients with WD compared to healthy subjects[12]. These findings were confirmed and correlated with the lipid profile in the liver and plasma of genetic mouse models of hepatic copper accumulation[13]. A study on organoids derived from IECs isolated from *Atp7b* global knockout mice identified lipid droplet accumulation in the IECs and evidence of aberrant processing of lipids in the same cells, findings that could be attributed to ATP7B

dysfunction in the intestinal epithelium[7]. Gut microbiota also affects lipid profile with consequences on liver pathology and regeneration[14]. An extensive study on mouse and rat models of WD and *in vitro* on human Caco-2 cells demonstrated increased lymphocyte infiltration in the small intestine and increased intestinal permeability with altered energy and lipid metabolism in intestinal homogenates[15]. However, it is unknown if metabolic changes in WD are related directly to intestinal ATP7B deficiency or if they are a consequence of hepatic copper accumulation and liver disease. To understand the effects of IEC ATP7B dysfunction on the intestine and liver, in the absence of hepatic copper accumulation, a mouse model with a targeted intestine-specific ATP7B knockout (*Atp7b*$^{\Delta IEC}$) was generated. This is important because copper is absorbed in the intestine; signs and symptoms of WD are also relevant to the gastrointestinal tract; and established anti-copper medications exert their action at the intestine level. In particular, zinc salts, which are frequently prescribed in the treatment of WD, act by inducing the synthesis of metallothioneins in the IECs which, in turn, block the intestinal absorption of dietary copper[16]. Recent studies on copper chelators in humans, demonstrated an unexpected mechanism of action with trientine tetrahydrochloride on inhibiting copper intestinal absorption[17]. With these premises, we hypothesized that intestinal ATP7B plays a role in modulating WD metabolic manifestations and liver disease. In the present study, *Atp7b*$^{\Delta IEC}$ mice were compared to *Atp7b* global knockout mice on a C57Bl/6 background (*Atp7b*$^{-/-}$) in a time-course study from 9 to 30 weeks of age. By exploring copper quantification, liver and intestine morphology, and liver and intestine RNA sequencing, we were ultimately able to identify pathways specifically affected by extra-hepatic ATP7B dysfunction.

MATERIALS AND METHODS

Animal models

All protocols were approved by the UC Davis Institutional Animal Care and Use Committee and followed the National Research Council's Guide for the Care and Use of Laboratory Animals.

126 *Atp7b*$^{\Delta IEC}$ model generation

127 As previously described[13], the UC Davis Mouse Biology Program generated *Atp7b*$^{\Delta IEC}$ mice using
128 B6.Cg-Tg(Vil1-cre)997Gum/J mice from the Jackson Laboratory (Bar Harbor, ME) and *Atp7b*$^{Lox/Lox}$
129 mice[18] kindly provided by Dr. Svetlana Lutsenko (Johns Hopkins University). Vil1-cre mice express Cre
130 recombinase in villus and crypt epithelial cells of the intestine under a villin-1 promoter. *Atp7b* gene
131 inactivation occurs by Cre-mediated removal of a 1.6 kb fragment in exon 2. Mice heterozygous for
132 *Atp7b* Lox and hemizygous for Vil1-cre ($Lox^{+/-}/Cre^{+}$) mice were produced and subsequently bred to
133 generate $Lox^{+/+}/Cre^{+}$, or *Atp7b*$^{\Delta IEC}$, mice. Intestinal epithelial cell (IEC)-specific *Atp7b* inactivation was
134 confirmed by gene and protein expression analysis (Supplemental Figure S1).

135 Animal husbandry and model characterization

136 The *Atp7b*$^{-/-}$ global knockout on a C57Bl/6 background was generated as previously described[18] and
137 kindly provided by Dr. Lutsenko. *Atp7b*$^{-/-}$ and *Atp7b*$^{\Delta IEC}$ colonies were bred and maintained on the UC
138 Davis campus in standard, open-top, plastic shoebox cages with Teklad TEK-Fresh bedding (Envigo,
139 Madison, WI) and nesting enrichment material under the following conditions: 20–23°C, 40%–65%
140 relative humidity, 14 h light/10 h dark light-cycle, and *ad libitum* LabDiet 5001 (PMI, St. Louis, MO)
141 and deionized water. Mice were housed 2-4 per cage. Colonies were maintained by hemizygous
142 (*Atp7b*$^{\Delta IEC}$) or heterozygous (*Atp7b*$^{-/-}$) breeding. *Atp7b*$^{-/-}$ and *Atp7b*$^{\Delta IEC}$ mice were co-housed with their
143 respective littermate controls and segregated by sex at weaning.

144 At 9, 16, 24, and 30 weeks of age, male and female *Atp7b*$^{-/-}$ and *Atp7b*$^{\Delta IEC}$ mice, and their respective
145 controls, had body weights measured prior to being anesthetized with isoflurane. Mice were then
146 exsanguinated retro-orbitally into K3EDTA collection tubes, euthanized by cervical dislocation, and
147 their livers and mesenteric white adipose tissue weighed and flash-frozen in liquid nitrogen. All samples
148 were collected between 9am and 11:30am. Blood samples were centrifuged at 6,000 x g for 10 minutes
149 and the plasma was aliquoted. All samples were stored at -80°C until further analysis.

150

IEC isolation

IECs were isolated as previously described[13]. Briefly, mice were anesthetized with isoflurane, then euthanized by cervical dislocation. A ventral incision site was made in the abdominal cavity and the small intestine removed and unfurled. The proximal half of the full small intestine length plus 2 cm was taken and further divided into 4 segments that were placed in a glass petri dish with ice-cold dissection buffer comprised of Hank's Balanced Salt Solution without calcium/magnesium, 10 mM HEPES, and 5% FBS. Each segment was flushed with ice-cold dissection buffer and any remaining pancreas and mesenteric fat were trimmed. Each segment was then cut open longitudinally, cut into ~0.5 cm pieces, placed in 40 ml dissociation buffer (HBSS without calcium/magnesium, 10mM HEPES, 12.5 mM EDTA, 5% FBS, 1mM dithiothreitol), and dissociated for 30 minutes at 300 rpm and 37°C. After passing the dissociated suspension through a 70 μm cell strainer and centrifuging, the supernatant was removed and the cell pellet washed with 3 rounds of 25 ml ice-cold PBS (pH 7.2) with 0.5% FBS and centrifugation. Live cells were counted and the cell suspension was aliquoted. Aliquots were centrifuged, supernatant was removed, and cell pellets were flash-frozen and stored at -80°C. All centrifugations were performed for 5 minutes at 300 x g and 4°C.

Liver and serum triglycerides and total cholesterol

For liver, 110 ± 10 mg of tissue was weighed and homogenized with sodium sulfate then transferred into a glass tube. Methanol (4 ml) and chloroform (8 ml) were added and the samples incubated overnight at 4°C. The next day, 2.4 ml of 0.7% NaCl solution was added to separate the chloroform phase and samples were incubated overnight at 4°C. The supernatant layer was aspirated and a 5 ml sample of the chloroform was evaporated under nitrogen gas then reconstituted with 0.4 ml of isopropanol. The reconstituted sample was assayed with Infinity reagents TR22421 and TR13421 from Fisher Diagnostics (Middletown, VA). For serum, 5 μl of sample was assayed in duplicate directly with the Fisher Diagnostics reagents.

Alanine transaminase (ALT) and ceruloplasmin activity levels in plasma

Samples for ALT were processed by the UC Davis Comparative Pathology Lab for analysis. Liver and kidney chemistries were analyzed on a Roche Integra 400+ (Roche Diagnostics, Indianapolis, IN) using Cobas assays by Roche Diagnostics for enzymes, substrates, and specific proteins. Ceruloplasmin ferroxidase activity was assayed using the Ceruloplasmin Colorimetric Activity Kit (Invitrogen, Carlsbad, CA) according to the manufacturer's protocol. Samples were diluted 1:20 in the provided assay buffer and a ceruloplasmin substrate was added. Plates were incubated at 30°C for 60 minutes followed by absorbance reading at 560 nm with a Synergy H1 microplate reader (Bio Tek, Winooski, VT).

RNA extraction and gene expression analysis

RNA isolation, cDNA generation, and qPCR were performed as previously described[19]. Briefly, RNA was isolated from 25 mg liver and $1x10^7$ IECs using the AllPrep RNA/DNA Mini kit (QIAGEN, Valencia, CA) according to the manufacturer's instructions. QIAGEN QIAshredder columns were used to homogenize IEC samples; liver samples were homogenized using a pellet pestle motor for 20 seconds (Fisher Scientific, Hampton, NH). RNA purity, concentration, and integrity were assessed by SpectraDrop Micro-Volume Microplate and Spectramax i3x plate reader (Molecular Devices, San Jose, CA) and agarose gel electrophoresis. The Superscript III First-strand Synthesis System (Invitrogen, Carlsbad, CA) was utilized to reverse-transcribe 5 μg RNA into cDNA. Quantitative PCR was run on a ViiA 7 Real-Time PCR System (Applied Biosystems, Foster City, CA) using SYBR Green master mix (Applied Biosystems, Foster City, CA) and a 1/25 cDNA dilution plated in triplicate along with a no-template control. *Gapdh* was used as a reference gene in IECs and *Ndufs3* in liver for *Atp7b* model validation.

RNA-sequencing analysis

RNA-seq library production, sequencing, and analysis were performed by Novogene Corporation, Inc. (Sacramento, CA) as previously described[20]. Briefly, the RNA Nano 6000 Assay Kit and Agilent Bioanalyzer 2100 system (Agilent Technologies, Inc., Santa Clara, CA) was used to assess RNA integrity and quantity. Sequencing libraries were generated using the NEBNext Ultra RNA Library Prep Kit for Illumina (New England Biolabs, Ipswich, MA) followed by size selection, amplification, and purification. Library preparations were sequenced on a NovaSeq 6000 S4 platform (Illumina, Inc., San Diego, CA), generating 150 bp paired-end reads. Raw reads were cleaned using fastp version 0.20.0 then aligned to GRCm38 mouse reference genome with Spliced Transcripts Alignment to a Reference software version 2.6.1d. Mapped reads were counted for each gene with FeatureCounts version 1.5.0-p3 and differential expression analysis of two conditions was performed using edgeR version 3.22.5. P-values were adjusted using the Benjamini & Hochberg method and ClusterProfiler R version 4.6.2 was used to test the statistical enrichment of differentially expressed genes in KEGG and Reactome pathways. Pathways with p-value less than 0.05 were considered significant. All sequencing data have been deposited in NCBI's BioSample database with BioProject ID PRJNA961737 (https://www.ncbi.nlm.nih.gov/bioproject/961737, access date 9/10/25) and GEO Submission-GSE279388 (https://www.ncbi.nlm.nih.gov/geo/query/acc.cgi?acc=GSE279388, access date 9/10/25).

Lysate preparation and western blot analysis

Frozen tissue was homogenized in RIPA buffer (150 mM NaCl, 1% NP-40, 0.5% sodium deoxycholate, 0.1% SDS, and 50 mM Tris–Cl pH 7.4) with Pierce EDTA-free Protease Inhibitor Tablets (ThermoFisher Scientific, Waltham, MA) and PhosStop phosphatase inhibitor (Roche, Mannheim, Germany) using a pellet pestle motor for 30 seconds (Fisher Scientific, Hampton, NH). Lysates were cleared by centrifugation at 15,000 × g, 4°C for 30 minutes. Lysates were frozen at -20°C prior to protein quantification utilizing a Pierce BCA Protein Assay Kit (ThermoFisher Scientific, Waltham, MA). Forty

µg protein was prepared with NuPage LDS sample buffer (Invitrogen, Waltham, MA), according to the manufacturer's protocols, without heating and was loaded into a 4%–12% Bolt Bis-Tris Plus protein gel (Invitrogen, Waltham, MA). Gels were run in MES buffer at 100V for 1 hour and transferred on a low fluorescence PVDF membrane using a Trans-Blot Turbo RTA Mini 0.45 µm LF PVDF Transfer Kit (Bio-Rad, Hercules, CA). Membranes were blocked with 5% Blotting-grade Blocker (Bio-Rad, Hercules, CA) in TBST for 1 hour at room temperature. Membranes were washed 3 x 5 minutes with TBST at room temperature and incubated with primary antibody in 5% BSA+TBST overnight at 4°C. Membranes were washed 3 x 5 minutes with TBST at room temperature and blotted with secondary antibody in 5% Blotting-grade Blocker in TBST for 1 hour at room temperature. Membranes were washed 3 x 5 minutes with TBST at room temperature prior to imaging on a ChemiDoc MP Imager (Bio-Rad, Hercules, CA). Primary antibodies used include anti-ATP7B (1: 1000, Abcam, Waltham, MA) and anti-β-actin (1:5000, Santa Cruz Biotechnology, Dallas, TX). Secondary antibodies used were goat anti-rabbit IgG Alexa Fluor Plus 800 (1:2500, Invitrogen, Waltham, MA) and goat anti-mouse IgG Alexa Fluor Plus 555 (1:2500, Invitrogen, Waltham, MA). Images were processed and densitometry analyzed using Image Lab software version 6.1.0 build 7 (Bio-Rad, Hercules, CA).

Copper quantification

Liver samples were digested in 4:1 trace metals grade concentrated nitric acid (Fisher Scientific, Hampton, NH) and hydrogen peroxide in a 65°C water bath then diluted to 10 ml with milli-Q water. Quantitative standards were made using a custom standard (Inorganic Ventures, Christiansburg, VA) diluted to create a 100 ng/g and a 2000 ng/g mixed element standard in 10.0% nitric acid (v/v). A calibration blank of 10.0% nitric acid (v/v) was used. Inductively coupled plasma mass spectrometry (ICP-MS) was performed on a Thermo iCapQ ICP-MS (Thermo Fisher Scientific, Waltham, MA) equipped with an ESI SC-2DX PrepFAST autosampler (Elemental Scientific Inc, Omaha, NE). A mixed element solution (IV-ICPMS-71D, Inorganic Ventures, Christiansburg, VA) was utilized as an internal

standard and added inline using the PrepFAST system. The isotope selected for analysis was 63,65Cu, as well as 45Sc, 89Y, and 115In (chosen as internal standards for data interpolation and machine stability). Data were calculated as µg copper per mg wet liver weight. Instrument performance is optimized daily through autotuning followed by verification via a performance report. Elemental analysis was performed at the Northwestern University Quantitative Bio-element Imaging Center, generously supported by the NIH under Grant S10OD020118.

Histology

All liver and intestine samples were fixed in 10% zinc formalin then paraffin-embedded, sectioned, and stained with H&E. Slide images were scanned with an Aperio AT2 slide scanner (Leica Biosystems, Deer Park, IL, USA). Slide images were stored and annotated on the UC Davis Aperio eSlide Manager online database hosted by Leica Biosystems. Slide section snapshots were acquired with Aperio ImageScope version 12.4.3.5008 (Leica Biosystems, Deer Park, IL, USA). Sample processing and pathologist evaluation were performed by the UC Davis Center for Genomic Pathology Laboratory.

Transmission electron microscopy (TEM)

After fixation in 2.5% glutaraldehyde and 2% paraformaldehyde in 0.1 M sodium phosphate buffer, tissues were rinsed twice in 0.1 M sodium phosphate buffer for a total of 30 minutes then placed in 1% osmium tetroxide in 0.1 M sodium phosphate buffer for 1 hour. Tissues were rinsed 2 x 15 minutes in 0.1 M sodium phosphate buffer then dehydrated in 50% ethanol, 75% ethanol, 95% ethanol (at least 30 minutes each) and finally in 100% ethanol (2 x 20 minutes). Tissues were then placed in propylene oxide (2 x 15 minutes). Samples were pre-infiltrated in half resin/half propylene oxide overnight. The next day, tissues were infiltrated in 100% resin (450 ml dodecenyl succinic anhydride, 250 ml Araldite 6005 epoxy resin, 82.5 ml Epon 812 embedding resin, 12.5 ml dibutyl phthalate, and 450 µl benzyldimethylamine) for 5 hours. Tissues were then embedded with fresh resin and polymerized at

65°C overnight. Embedded tissues were sectioned with a Leica EM UC6 ultramicrotome at a thickness of 90 nm and collected on copper mesh grids. Sections were stained with 4% aqueous uranyl acetate for 20 minutes and for 2 minutes in 0.2% lead citrate in 0.1 N sodium hydroxide. TEM imaging was done on a FEI Talos L120C at 80 kv using a Thermo Scientific Ceta 16MP camera (Thermo Fisher Scientific, Waltham, MA). All samples were processed and imaged by the UC Davis Biological Electron Microscopy Facility.

RESULTS

Body weights, tissue weight ratios, and ALT

Male and female *Atp7b*$^{-/-}$ mice showed normal body weight compared to respective WT mice until 30 weeks of age when both male and female *Atp7b*$^{-/-}$ mice started to present lower body weight compared to WT (Table 1). At 9, 16, 24, and 30 weeks of age, both WT and *Atp7b*$^{-/-}$ female mice weighed less than their male counterparts, as expected. Tissue weights for both liver and mesenteric white adipose tissue (MWAT) (Supplemental Table S1) were normalized by body weight. *Atp7b*$^{-/-}$ female mice had higher liver weight ratios at 16, 24, and 30 weeks of age, whereas the increase did not manifest in male *Atp7b*$^{-/-}$ until 24 weeks. A significant decrease in MWAT ratio was observed in *Atp7b*$^{-/-}$ male mice at 30 weeks. Female *Atp7b*$^{-/-}$ mice had a significant decrease in MWAT ratio at 24 weeks. Interestingly, sex differences in MWAT ratio were only seen at 30 weeks, with female WT mice having significantly lower MWAT ratio relative to male WT mice. This difference in 30-week-old WT females may explain the lack of significant MWAT difference between 30-week *Atp7b*$^{-/-}$ and WT female mice. Significant increases in ALT levels were seen in both male and female *Atp7b*$^{-/-}$ mice starting at 16 weeks relative to WT and persisted in both sexes through 30 weeks of age (Table 2). Sex dependent differences in ALT levels were only seen between male and female mice at 24 weeks. Ceruloplasmin activity levels did not show consistent or significant differences except for a significant reduction in 16-week-old *Atp7b*$^{-/-}$ females compared with WT.

In contrast to the *Atp7b*$^{-/-}$ mice, *Atp7b*$^{\Delta IEC}$ mice did not show significant changes in body weight or liver weight compared to their respective iWT (Supplemental Table S1). Male *Atp7b*$^{\Delta IEC}$ mice presented a significantly lower body weight only at 9 weeks, compared to iWT mice. This difference is likely due to higher-than-average body weight in iWT mice rather than a failure for *Atp7b*$^{\Delta IEC}$ mice to gain weight which is further confirmed by a lack of difference in weight at later time points. As expected, *Atp7b*$^{\Delta IEC}$ and iWT female mice have lower body weight than males at 9, 16, 24, and 30 weeks. Differences in MWAT ratio are sex dependent; female iWT have significantly decreased values at 16 weeks compared with male iWT mice as do female *Atp7b*$^{\Delta IEC}$ and iWT mice at 24 weeks compared with their respective male counterparts. Additionally, the increase in serum ALT levels seen in *Atp7b*$^{-/-}$ mice did not occur in *Atp7b*$^{\Delta IEC}$ mice.

Copper quantification

ICP-MS was utilized for copper analysis in both liver and IECs of both mouse models. In agreement with previous studies[21], hepatic copper accumulation was seen in both male and female *Atp7b*$^{-/-}$ mice relative to WT at all times points, with copper levels 15- to 25-fold higher in *Atp7b*$^{-/-}$ mice (Figure 1A, 1C). Hepatic copper accumulation was highest at 9 weeks and remained at least 15 times higher in *Atp7b*$^{-/-}$ mice compared with WT despite a progressive reduction over time. Copper levels were not different in the liver of *Atp7b*$^{\Delta IEC}$ mice or the IECs of either *Atp7b*$^{-/-}$ or *Atp7b*$^{\Delta IEC}$ mice, relative to their respective controls (Figure 1B, 1D).

Liver and serum total cholesterol and triglycerides

Given evidence of altered lipid processing in the intestine of *Atp7b*$^{-/-}$ mice[7, 13, 15], serum and liver cholesterol and triglyceride (TG) levels were evaluated. Both serum cholesterol and serum TG levels trended downward over time in *Atp7b*$^{-/-}$ male and female mice (Figure 2A-2D). At 24 and 30 weeks, serum cholesterol and TG levels were significantly decreased in both male and female *Atp7b*$^{-/-}$ mice

relative to WT. Serum cholesterol showed up to a 3-fold decrease between *Atp7b*$^{-/-}$ and WT mice, while serum TG showed up to a 2.7-fold decrease. Liver cholesterol levels were statistically increased at 16 and 24 weeks in male and female *Atp7b*$^{-/-}$ mice (Figure 2E, 2G). In contrast, liver TG levels were decreased at all time points with more significant decreases occurring with age progression (Figure 2F, 2H). By 30 weeks of age, there was a 2-fold decrease in liver TG levels in both male and female *Atp7b*$^{-/-}$ mice compared to WT mice.

Atp7b$^{\Delta IEC}$ mice did not show any differences in serum or liver cholesterol and TG levels in either male or female mice relative to iWT at all time points, except for an increased TG at 9 weeks in female *Atp7b*$^{\Delta IEC}$ relative to iWT. The increase in TG did not persist at later time points and was not seen in male mice (Figure 2A-2H).

Liver histology

From 9 to 30 weeks of age, H&E staining of WT mice show hepatocytes with a relatively uniform nuclear and hepatocellular size and shape with no inflammation and only mild cytoplasmic glycogenosis by 30 weeks (Figure 3A, 3C, 3E, 3G). In contrast, nuclear and hepatocyte enlargement and nuclear glycogenosis are already evident in *Atp7b*$^{-/-}$ mice at 9 weeks of age and continue to increase with age (Figure 3B, 3D, 3F, H). While not present at 9 weeks, lobular inflammation begins to manifest by 16 weeks. By 30 weeks of age, *Atp7b*$^{-/-}$ livers, on average, present with moderate lobular and periportal inflammatory infiltrate.

Unlike the global *Atp7b*$^{-/-}$ model with liver disease, iWT (Figures 4A, 4C, 4E, 4G) and *Atp7b*$^{\Delta IEC}$ (Figure 4B, 4D, 4F, 4H) livers display a phenotype similar to WT controls from 9 to 30 weeks of age, regarding nuclear and hepatocellular morphology. However, both *Atp7b*$^{\Delta IEC}$ and iWT hepatocytes exhibit a greater degree of cytoplasmic glycogenosis. At 9 weeks, mild glycogenosis is already present, peaking at about 24 weeks of age and then appears attenuated by 30 weeks.

Intestine histology

H&E staining of global *Atp7b*$^{-/-}$ (Figure 5B) and *Atp7b*$^{\Delta IEC}$ (Figure 5F) proximal intestine reveals normal pathology at 16 weeks of age compared to respective controls, WT (Figure 5A) and iWT (Figure 5E). The villi are normal with no signs of intra-epithelial lymphocytes, lamina propria inflammation, or crypt hyperplasia. The epithelial barrier remains intact and the enterocytes and microvilli are well-preserved. At 24 weeks of age, slight to mild multifocal lamina propria inflammation with mild distortion of the villous base is observed in all genotypes, WT (Figure 5C) vs. *Atp7b*$^{-/-}$ (Figure 5D) and iWT (Figure 5G) vs. *Atp7b*$^{\Delta IEC}$ (Figure 5H).

TEM IEC Mitochondria

A preliminary survey of duodenal intestine from both *Atp7b*$^{-/-}$ and *Atp7b*$^{\Delta IEC}$ mice at 16 and 24 weeks of age showed alterations in mitochondria structure and matrix content. Compared with WT (Figure 6A), *Atp7b*$^{-/-}$ mice had a high frequency of intestinal mitochondria with unorganized or depleted cristae, electron-translucent matrices, and ballooning (Figure 6C, 6E). *Atp7b*$^{-/-}$ mice also had occasional mitochondria with vesicular cristae (Figure 6C, 6E, arrows) and U-shaped morphology (Figure 6G), in contrast to WT mice which had none.

Atp7b$^{\Delta IEC}$ mice had similar intestinal mitochondria alterations (Figure 6D, 6F) as the *Atp7b*$^{-/-}$ mice when compared with their iWT counterparts (Figure 6B), regarding unorganized or depleted cristae, electron-translucent matrices, and ballooning; however, compromised outer membrane integrity appeared more exacerbated in *Atp7b*$^{\Delta IEC}$ mice. Despite ballooning likely due to outer membrane damage/leakage, *Atp7b*$^{-/-}$ mitochondria maintain a relatively smooth border, whereas *Atp7b*$^{\Delta IEC}$ mitochondria, particularly at 16 weeks, have a more distorted border, creating irregular gaps between the inner and outer membranes (Figure 6D). At 16 weeks, *Atp7b*$^{\Delta IEC}$ mitochondria also frequently present with dilated cristae that sometimes appear vesicular; dilated cristae are also observed at 24 weeks but dilation is much milder and significantly less frequent (Figure 6D, 6H, arrows).

TEM IEC barrier

In addition to mitochondria, alterations to the IEC apical junctional complex (tight junction, adherens junction, desmosome) and intercellular membrane adhesion were also examined. Compared with their WT (Figure 7A) or iWT (Figure 7B) controls, both *Atp7b*$^{-/-}$ and *Atp7b*$^{\Delta IEC}$ mice exhibit multiple instances of single-sided desmosomes[15] (Figure 7C, 7D), both as part of the junctional complex and other desmosomes along the lateral membranes; in some instances of the junctional complex, there appears to be no desmosome following the adherens junction. Even when double-sided, desmosome proteins are frequently less electro-dense and/or are diffuse, appearing like an unorganized protein cloud instead of the more electro-dense plaque. At 16 weeks of age, *Atp7b*$^{-/-}$ mice also frequently display adherens junctions and desmosomes that are abnormally wide (Figure 7E); this also occurs in *Atp7b*$^{\Delta IEC}$ mice, though mostly with just desmosomes and not until 24 weeks (Figure 7F). In *Atp7b*$^{-/-}$ mice, the lateral membranes often loop back and forth excessively with irregular and abnormally wide intercellular adhesion spaces (Figure 7G), compared with WT. *Atp7b*$^{\Delta IEC}$ mice, however, rarely have the excessively looping lateral membranes and the intercellular adhesion space between cells is consistent with their iWT counterpart (Figure 7H).

RNA-sequencing and pathway analyses

RNA-sequencing was performed in liver and isolated IECs of both mouse strains at 16 and 30 weeks of age. The two time points were selected based on significant hepatic copper accumulation in *Atp7b*$^{-/-}$ mice and liver histology which is expected to progress from lack of fibrosis at week 16 to stage 3-4 fibrosis with regenerative nodules at week 30.

KEGG Pathway Analyses

KEGG pathway analyses were performed on IECs of *Atp7b*$^{-/-}$ and *Atp7b*$^{\Delta IEC}$ mice relative to their respective controls at both 16 and 30 weeks of age. At 16 weeks of age, *Atp7b*$^{-/-}$ mice revealed several

differentially regulated pathways, with NOD-like receptor signaling being the pathway represented by the highest number of genes (Supplemental Figure S2A, Supplemental Table S2). Genes related to lipid metabolism and mineral absorption, including fat digestion and absorption, were also differentially regulated. Similar to *Atp7b*$^{-/-}$ mice, *Atp7b*$^{\Delta IEC}$ mice showed involvement of NOD-like receptor signaling pathway and changes in fat digestion, however, the specific pathways and genes affected were different (Supplemental Figure S2B, Supplemental Table S3). The number of differentially expressed genes was significantly lower in *Atp7b*$^{\Delta IEC}$ compared to *Atp7b*$^{-/-}$ mice, with 347 differentially expressed genes in *Atp7b*$^{\Delta IEC}$ mice compared to 1576 in *Atp7b*$^{-/-}$ mice. At 30 weeks, the differentially expressed pathways in both *Atp7b*$^{-/-}$ and *Atp7b*$^{\Delta IEC}$ mice included non-alcoholic fatty liver disease (now named metabolism-associated steatotic liver disease, MASLD), oxidative phosphorylation, chemical carcinogenesis via reactive oxygen species, and prion disease pathways (Supplemental Figure S3, Supplemental Tables S4 and S5). Two genes that appear as a common thread between these pathways and others listed are mechanistically relevant mitochondrially encoded cytochrome c oxidase III, *mt-Co3*, cytochrome b, and *mt-Cytb*, both related to mitochondria electron transport.

For KEGG pathway analyses in the liver at 16 weeks, changes in cell cycle, fatty acid metabolism, oxidative phosphorylation, and AMPK signaling were observed in *Atp7b*$^{-/-}$ mice (Supplemental Figure S4A, Supplemental Table S6) and are in agreement with previous studies[22]. Interestingly, in spite of normal hepatic *Atp7b* expression levels and lack of hepatic copper accumulation, *Atp7b*$^{\Delta IEC}$ mouse livers still presented with changes in gene expression profiles (Supplemental Figure S4B, Supplemental Table S7), although with fewer dysregulated genes and affected pathways compared to *Atp7b*$^{-/-}$ mice. Specifically, affected pathways included DNA replication and AMPK, MAPK, and PPARα signaling. By 30 weeks of age, *Atp7b*$^{-/-}$ mice still showed changes in pathways differentially regulated at 16 weeks, however, with a greater number of differentially expressed genes in those same pathways, likely due to the progression of liver disease (Supplemental Figure S5A, Supplemental Table S8). In contrast, while the dysregulated pathways at 16 weeks remained differentially expressed over time, *Atp7b*$^{\Delta IEC}$ mice did

not show increases in the numbers of genes affected (Supplemental Figure S5B, Supplemental Table S9).

Lipid Metabolism in the IECs of Atp7b$^{-/-}$ and Atp7b$^{\Delta IEC}$ mice

IEC lipid metabolism pathways were affected at 16 and 30 weeks of age in both *Atp7b*$^{-/-}$ and *Atp7b*$^{\Delta IEC}$ mice. Fatty acid digestion and metabolism and linoleic acid metabolism pathways were differentially expressed in both knockout models at 16 weeks of age (Supplemental Figure S6A-S6B). Although there was partial overlap in the affected pathways, the specific dysregulated genes were mostly different between the two strains. Compared to respective WT mice, lipid metabolism pathways in *Atp7b*$^{-/-}$ mice showed increased expression of diacylglycerol O-acyltransferase (*Dgat2*), acyl-CoA dehydrogenase long chain (*Acadl*), and fatty acid desaturase 6 (*Fads6)*, all involved in the synthesis of fatty acids (Supplemental Figure S6C-S6E). Additionally, *Atp7b*$^{-/-}$ mice exhibited a decrease in acetyl-Coenzyme A acetyltransferase 1 (*Acat1*), which encodes for the protein involved in the last step of ketolysis during fat processing. In *Atp7b*$^{\Delta IEC}$ mice, the genes driving altered lipid metabolism included down-regulated aldehyde dehydrogenase 7 family member A1 (*Aldh7a1)*, which plays a major role in the detoxification of aldehydes, and up-regulated solute carrier family 27 member 2 (*Slc27a2)*, which converts long-chain free fatty acids into fatty acyl-CoA esters (Supplemental Figure S6F-S6G). At 30 weeks of age, the trends persisted with *Atp7b*$^{-/-}$ and *Atp7b*$^{\Delta IEC}$ mice showing alterations in lipid metabolism pathways but, again, with different specific genes identified (Supplemental Figure S7A-S7B). Increased expression of *Acadl*, stearoyl-Coenzyme A desaturase 2 (*Scd2*), and acetyl-CoA acyltransferase 1 (*Acaa1*) was shown in *Atp7b*$^{-/-}$ mice, all of which play a role in lipid biosynthesis (Supplemental Figure S7C-S7E). *Atp7b*$^{\Delta IEC}$ mice instead presented increased expression of microsomal triglyceride transfer protein (*Mttp*) and monoacylglycerol O-acyltransferase 2 (*Mogat2)*, both central in TG synthesis (Supplemental Figure S7F-S7G). Of note, at 30 weeks, IECs from *Atp7b*$^{-/-}$ mice were compared to heterozygous mice instead of WT mice due to lack of WT mice in the breeding colony.

AMPK Signaling in the liver of Atp7b$^{-/-}$ and Atp7b$^{\Delta IEC}$ mice

In contrast to the IECs, changes in liver pathways were driven by overlapping genes in both *Atp7b*$^{-/-}$ and *Atp7b*$^{\Delta IEC}$ mice, although with different numbers of involved genes. While both knockout models displayed differentially expressed genes in the AMPK signaling pathway at 16 weeks, *Atp7b*$^{-/-}$ mice had 81 genes differentially expressed, whereas *Atp7b*$^{\Delta IEC}$ mice presented only 8, with similar trends between the two strains (Figure 8, 9A). In particular, stearoyl-coenzyme A desaturase 3 (*Scd3*), which enables palmitoyl-CoA 9-desaturase activity and is homologous to human stearoyl-coenzyme A desaturase, and *Scd*, which catalyzes the rate-limiting step in the formation of monounsaturated fatty acids, was up-regulated in both *Atp7b*$^{-/-}$ and *Atp7b*$^{\Delta IEC}$ mice (Figure 9B). Additionally, both *Atp7b*$^{-/-}$ and *Atp7b*$^{\Delta IEC}$ mice presented decreased expression of lipase hormone (*Lipe*), which enables carboxylic ester hydrolase activity, protein kinase binding activity, and serine hydrolase activity, as well as decreased expression of acyl-CoA synthetase long-chain family member 3 (*Acsl3*), which converts long-chain free fatty acids into fatty acyl-CoA esters in fatty acid metabolism (Figure 9C, 9D). The human ortholog of this protein, lipase E, hydrolyzes stored TGs to free fatty acids. At 30 weeks, both knockout models showed persistent changes in the AMPK signaling pathway (Figure 10, 11A). Sterol regulatory element binding transcription factor 1 (*Srebf1*) transcript levels were reduced in both *Atp7b*$^{-/-}$ and *Atp7b*$^{\Delta IEC}$ mice (Figure 11B).

Cell Cycle and DNA Replication in the IECs of Atp7b$^{-/-}$ *and Atp7b*$^{\Delta IEC}$ *mice*

Reactome pathway analysis revealed changes in genes related to cell cycle and DNA synthesis and replication in the IECS of *Atp7b*$^{-/-}$ and *Atp7b*$^{\Delta IEC}$ mice at 16 (Supplemental Figure S8A-S8B) and 30 (Supplemental Figure S8C-S8D) weeks of age, and both strains showed an overall down-regulation of genes associated with cell cycle and DNA replication/repair activities. At 16 weeks, *Atp7b*$^{-/-}$ mice showed changes in expression of genes associated with cell cycle (*Cdc20, Cdca8*) and centromere genes (*Cenpa, Cenpe, Cenph, Cenpm*) (Supplemental Table S10), both of which are essential in cell division. In contrast, *Atp7b*$^{\Delta IEC}$ mice at 16 weeks had very few differentially expressed genes though they were still histone and cell cycle-associated genes (Supplemental Table S11). By 30 weeks of age, both mouse

476 strains showed significant changes in cell cycle and DNA replication pathways relative to their respective
477 controls. *Atp7b*$^{-/-}$ mice still exhibited differential expression in genes associated with cell division and
478 the centromere but shifted to genes related specifically to chromatid cohesion (Supplemental Table S12).
479 At 30 weeks *Atp7b*$^{\Delta IEC}$ mice have a significant number of cell cycle and DNA damage response-related
480 genes differentially expressed compared with iWT, including increased expression of several genes
481 encoding proteosome subunits (e.g., *Psme1, Psmb4, Psmb8, Psmb10, Psmc5*) (Supplemental Table S13).
482

483 **DISCUSSION**

484 In this time-course study, we aimed to characterize a new mouse model with an intestine-specific *Atp7b*
485 knockout. The following key findings were identified: 1) *Atp7b* dysfunction causes mitochondrial and
486 junctional abnormalities in the intestine; 2) *Atp7b* dysfunction is associated with differential expression
487 of pathways and genes related to inflammation, mitochondrial function, lipid metabolism, cell cycle, and
488 prion disease in the IECs and in the liver; 3) dysregulated pathways and genes are independent from
489 hepatic copper accumulation or altered liver pathology; and 4) *Atp7b*$^{-/-}$ mice present changes in
490 pathways, including MASLD, that partially overlap between the intestine and the liver. WD is a
491 monogenic disease with systemic manifestations, likely due to the interactions between genetic,
492 epigenetic, and metabolic factors[20, 23]. However, the role of extra-hepatic ATP7B on WD systemic
493 manifestations and liver disease remains unknown. In the absence of copper accumulation and related
494 organ-specific inflammation, we show intestinal ATP7B contributes to the pathophysiology of WD and
495 possibly influences the response to anti-copper treatment. The interaction between the intestine and the
496 liver is crucial in liver diseases and is increasingly recognized in WD. Alcohol-associated liver disease
497 presents increased intestinal permeability with bacterial component translocation, including
498 lipopolysaccharides, which, in turn, induces liver inflammation through increased tumor necrosis factor
499 expression in the liver and thus driving progression of liver disease[24, 25]. MASLD is similarly associated
500 with intestinal barrier dysfunction, higher levels of circulating bacterial endotoxin[26], and changes in the

gut microbiota[27, 28]. Adding to this, Parkinson's disease, which is routinely considered in the differential diagnosis of neurological WD, is also characterized by gut dysbiosis[29]. WD has liver and intestine morphological features shared with common liver diseases but also features unique to this rare condition. We observed marked mitochondrial morphological abnormalities in the IECs of *Atp7b*$^{-/-}$mice, concomitant with hepatic copper accumulation, and in the IECs of *Atp7b*$^{\Delta IEC}$ mice, without copper accumulation. In addition, junctional changes in the intestine of both mouse models were observed. Mitochondrial abnormalities have been previously reported in mouse models of hepatic copper accumulation, mostly focused on the hepatocytes[30]. Fontes et al. described altered mitochondrial structures in the intestine of two rodent models with WD and Caco-2 ATP7B KO cells. Rats with hepatic copper accumulation have intestine mitochondria with depleted and unorganized cristae, loss of electron dense matrices, and detached outer mitochondria membranes[15]. Functionally, in the same study, authors reported increased intestinal permeability in the WD rat model of acute hepatitis, with *in vivo* findings supported by *in vitro* experiments in Caco-2 cells. Intestinal tissue proteomics analysis identified proteins involved in lipid metabolism and glycolysis as being dysregulated[15]. Sarode et al. described a specific lipidomic pattern in the liver and plasma of *Atp7b*$^{\Delta IEC}$ mice characterized by dysregulated triglyceride, diglyceride, phospholipid, and sphingolipid metabolism, with evidence of abnormal response to a high-fat dietary challenge[13]. In this study, there was evidence of a functional correlation between gut microbiota changes and lipidomic patterns. Intestine involvement in WD pathogenesis was previously explored by Pierson et al. who showed that organoids derived from *Atp7b*$^{-/-}$ mouse IECs presented impaired lipid processing with mislocalization of apolipoprotein B and loss of chylomicron development[7]. These studies showed intestinal copper metabolism changes present early in the course of liver disease, although there is always significant presence of hepatic copper accumulation. The next important step is understanding to what extent the liver pathology is affected and potentially regulated by these intestinal metabolic changes. In the current study, RNA-sequencing of 16-week-old *Atp7b*$^{-/-}$ mice showed IEC changes in fat digestion- and absorption-related genes. This finding was accompanied

by misregulation of hepatic fatty acid metabolism and degradation pathways. By 30 weeks of age, the pathways affected in the intestine shift toward chemical carcinogenesis and oxidative phosphorylation, both of which are indicative of mitochondrial damage. This was accompanied by increasing liver disease severity and changes in pathways, including chemical carcinogenesis and non-alcoholic fatty liver disease/MASLD. RNA-sequencing of *Atp7b*$^{\Delta IEC}$ mouse IECs revealed similar changes to those seen in *Atp7b*$^{-/-}$ mice, although with a smaller number of involved genes. IECs from 16-week-old *Atp7b*$^{\Delta IEC}$ mice showed changes in gene transcripts related to lipid metabolism accompanied by changes in several hepatic signaling pathways, including MAPK and AMPK. At 30 weeks of age, the IEC pathways altered in *Atp7b*$^{\Delta IEC}$ mice included chemical carcinogenesis and oxidative phosphorylation, similar to *Atp7b*$^{-/-}$ IECs. Pathways affected in the liver of *Atp7b*$^{\Delta IEC}$ mice at 30 weeks include AMPK signaling and MASLD, which are seen in *Atp7b*$^{-/-}$ mice at 30 weeks as well. These results suggest the metabolic pathway changes seen in the liver of *Atp7b*$^{-/-}$ mice are at least partially driven by the gut-liver axis, independent from hepatic copper accumulation. A study on *Atp7b*$^{-/-}$ mice previously identified increased hepatic phosphorylated AMPK levels[22]. Notably, AMPK is a major sensor of oxidative stress[31], as induced by copper accumulation, and has been connected to dysregulation of lipid metabolism. The finding of dysregulated AMPK pathway both in the IECs and the liver confirms that the source of aberrant lipid metabolism is actually localized in the gastrointestinal tract. Pathways that need to be mentioned as they are likely to have pathogenic relevance include NOD-like receptor signaling pathway, prion disease, cell cycle, and DNA replication. In particular, NOD-like receptor signaling reflects inflammasome activation and could be linked to altered gut microbiota[32, 33]. Of note, marked dysregulation of this pathway in IECs of both *Atp7b*$^{-/-}$ and *Atp7b*$^{\Delta IEC}$ mice at 16 weeks of age was observed. Prion protein has been shown to favor copper toxicity and its suppression is a possible therapeutic target in WD[34]. Prion protein was identified through genome-wide screening in ATP7B-KO HepG2 cells and we identified prion disease pathway dysregulation both in IECs and livers of both mouse models.

The other major pathways identified by RNA-sequencing analysis relates to cell cycle and DNA replication. Changes in cell cycle, mitosis, and nuclear division are well-described in livers of mouse models and in patients with WD[35, 36] and we confirmed the involvement of these pathways in the livers of both mouse models. It is important to note that liver and IEC transcriptome findings were not associated with significant changes in liver pathology, liver enzymes, or cholesterol or triglyceride levels in *Atp7b*$^{\Delta IEC}$ mice, suggesting that ultimately hepatic copper accumulation is the determinant factor for the progression of liver disease. In addition, there was no evidence of increased intestinal copper in *Atp7b*$^{\Delta IEC}$ mice, which is in agreement with previous findings of lack of total copper changes in the intestine of *Atp7b*$^{-/-}$ rats[15]. The lack of total copper accumulation could be due to redistribution of copper in subcellular compartments. The present study had several strengths, including the time-course assessment of a new mouse model and the fact that we conducted RNA-sequencing analyses specifically on IECs rather than the whole intestine, with consequent detailed characterization of the cellular subtype driving the metabolic changes. Ultimately, this study points to the fact that the pathogenesis of liver disease in WD is affected by ATP7B dysregulation in the intestine as the first site of lipid metabolism and other mechanistically relevant pathways and genes. The clinical implications of these findings are several. Nutrients and dietary components are likely to interact with ATP7B copper transporter, not only at the level of dietary copper content but relatively to fat intake. Zinc salts and chelators exert their action at the level of the intestine and it is possible that *ATP7B* variants interact or interfere in different ways with anti-copper drugs, potentially explaining variable treatment response. Finally, the interactions between intestinal function and permeability, gut microbiota, and intestinal ATP7B dysfunction affect the liver and the brain in WD, more so than any other metabolic liver disease, and are to be seen as new potential therapeutic sites. Treatment options targeted to the intestinal barrier or dietary modifications focused on energy metabolism modulation should be studied in patients with WD, especially when presenting with hepatic steatosis or poor response to conventional copper lowering strategies. Future studies should include intestine biopsies from patients with WD to explore their morphology and

ultrastructure and should plan for dietary interventions based on energy metabolism modulation. The field is rapidly evolving and the present data help with the identification of the intestine as a therapeutic site. In previous studies, human induced pluripotent stem cell-derived hepatocytes have been successfully generated for drug screening or therapeutic purposes in WD[37-41]. In particular, CRISPR-targeted genome editing has successfully edited *ATP7B* variants in pluripotent stem cells derived from patients with WD [40]. A lentiviral vector-based approach was used to correct ATP7B function in hepatocyte-like cells derived from WD patients[37]. It is possible that IECs can be generated to rescue dysfunctional IECs in WD patients. Ultimately, WD-specific edited hepatocytes and IECs could restore organ-specific ATP7B dysfunction. In conclusion, WD should be managed as a systemic disease with varied clinical presentations and variable response to anti-copper treatments likely due to the occurrence of multiple factors, including extra-hepatic ATP7B dysfunction.

Authors Contributions

A.C. and N.M.S. performed experiments, analyzed the data, and wrote the manuscript; C. D.G., G.V.S., H.H., and M.B. contributed to the experiments, data analysis and interpretation, and reviewed the manuscript; A. F., H. Z., S.L., and M.H. contributed to data analysis and interpretation, and reviewed the manuscript; V.M. secured funding, designed the experiment, contributed to data analysis and interpretation, and wrote the manuscript.

Ethical assurance

V.M. is the guarantor of this work and, as such, had full access to all of the data in the study and takes responsibility for the integrity of the data and the accuracy of the data analysis.

REFERENCES

[1] Chen L, Min J, Wang F: Copper homeostasis and cuproptosis in health and disease. Signal Transduct Target Ther 2022, 7:378.

[2] Sailer J, Nagel J, Akdogan B, Jauch AT, Engler J, Knolle PA, Zischka H: Deadly excess copper. Redox Biol 2024, 75:103256.

[3] Pierson H, Yang H, Lutsenko S: Copper Transport and Disease: What Can We Learn from Organoids? Annu Rev Nutr 2019, 39:75-94.

[4] Nose Y, Kim BE, Thiele DJ: Ctr1 drives intestinal copper absorption and is essential for growth, iron metabolism, and neonatal cardiac function. Cell Metab 2006, 4:235-44.

[5] Moriya M, Ho YH, Grana A, Nguyen L, Alvarez A, Jamil R, Ackland ML, Michalczyk A, Hamer P, Ramos D, Kim S, Mercer JF, Linder MC: Copper is taken up efficiently from albumin and alpha2-macroglobulin by cultured human cells by more than one mechanism. Am J Physiol Cell Physiol 2008, 295:C708-21.

[6] Lutsenko S, Barnes NL, Bartee MY, Dmitriev OY: Function and regulation of human copper-transporting ATPases. Physiol Rev 2007, 87:1011-46.

[7] Pierson H, Muchenditsi A, Kim BE, Ralle M, Zachos N, Huster D, Lutsenko S: The Function of ATPase Copper Transporter ATP7B in Intestine. Gastroenterology 2018, 154:168-80.e5.

[8] Hassan MK, Alswat K, El-Kassas M: Shedding lights on diagnostic challenges in Wilson's disease: The positive impact of introducing steatotic liver disease new nomenclature umbrella. Liver Int 2024, 44:1267-8.

[9] Fanni D, Guido M, Gerosa C, Vallascas V, Moi M, Coni P, Vallebona E, Van Eyken P, Barcellona D, Scano A, Orrù G, Pampaloni P, Castagnola M, Faa G: Liver changes in Wilson's disease: the full spectrum. A report of 127 biopsies from 43 patients. Eur Rev Med Pharmacol Sci 2021, 25:4336-44.

[10] Hunt DP, Sahani DV, Corey KE, Masia R: Case records of the Massachusetts General Hospital. Case 30-2014. A 29-year-old man with diarrhea, nausea, and weight loss. N Engl J Med 2014, 371:1238-47.

[11] Medici V, Kebede N, Stephens J, Kunjappu M, Vierling JM: Clinical signs and symptoms of Wilson disease in a real-world cohort of patients in the United States: a medical chart review study. Frontiers in Gastroenterology 2024, 2.

[12] Cai X, Deng L, Ma X, Guo Y, Feng Z, Liu M, Guan Y, Huang Y, Deng J, Li H, Sang H, Liu F, Yang X: Altered diversity and composition of gut microbiota in Wilson's disease. Sci Rep 2020, 10:21825.

[13] Sarode GV, Mazi TA, Neier K, Shibata NM, Jospin G, Harder NHO, Caceres A, Heffern MC, Sharma AK, More SK, Dave M, Schroeder SM, Wang L, LaSalle JM, Lutsenko S, Medici V: The role of intestine in metabolic dysregulation in murine Wilson disease. Hepatol Commun 2023, 7.

[14] Yin Y, Sichler A, Ecker J, Laschinger M, Liebisch G, Höring M, Basic M, Bleich A, Zhang XJ, Kübelsbeck L, Plagge J, Scherer E, Wohlleber D, Wang J, Wang Y, Steffani M, Stupakov P, Gärtner Y, Lohöfer F, Mogler C, Friess H, Hartmann D, Holzmann B, Hüser N, Janssen KP: Gut microbiota promote liver regeneration through hepatic membrane phospholipid biosynthesis. J Hepatol 2023, 78:820-35.

[15] Fontes A, Pierson H, Bierła JB, Eberhagen C, Kinschel J, Akdogan B, Rieder T, Sailer J, Reinold Q, Cielecka-Kuszyk J, Szymańska S, Neff F, Steiger K, Seelbach O, Zibert A, Schmidt HH, Hauck SM, von Toerne C, Michalke B, Semrau JD, DiSpirito AM, Ramalho-Santos J, Kroemer G, Polishchuk R, Azul AM, DiSpirito A, Socha P, Lutsenko S, Zischka H: Copper impairs the intestinal barrier integrity in Wilson disease. Metabolism 2024, 158:155973.

[16] Sturniolo GC, Mestriner C, Irato P, Albergoni V, Longo G, D'Incà R: Zinc therapy increases duodenal concentrations of metallothionein and iron in Wilson's disease patients. Am J Gastroenterol 1999, 94:334-8.

649 [17] Kirk FT, Munk DE, Swenson ES, Quicquaro AM, Vendelbo MH, Schilsky ML, Ott P, Sandahl TD:
650 Effects of trientine and penicillamine on intestinal copper uptake: A mechanistic 64 Cu PET/CT study
651 in healthy humans. Hepatology 2024, 79:1065-74.
652 [18] Muchenditsi A, Yang H, Hamilton JP, Koganti L, Housseau F, Aronov L, Fan H, Pierson H,
653 Bhattacharjee A, Murphy R, Sears C, Potter J, Wooton-Kee CR, Lutsenko S: Targeted inactivation of
654 copper transporter Atp7b in hepatocytes causes liver steatosis and obesity in mice. Am J Physiol
655 Gastrointest Liver Physiol 2017, 313:G39-g49.
656 [19] Medici V, Sarode GV, Napoli E, Song GY, Shibata NM, Guimarães AO, Mordaunt CE, Kieffer
657 DA, Mazi TA, Czlonkowska A, Litwin T, LaSalle JM, Giulivi C: mtDNA depletion-like syndrome in
658 Wilson disease. Liver Int 2020, 40:2776-87.
659 [20] Sarode GV, Neier K, Shibata NM, Shen Y, Goncharov DA, Goncharova EA, Mazi TA, Joshi N,
660 Settles ML, LaSalle JM, Medici V: Wilson Disease: Intersecting DNA Methylation and Histone
661 Acetylation Regulation of Gene Expression in a Mouse Model of Hepatic Copper Accumulation. Cell
662 Mol Gastroenterol Hepatol 2021, 12:1457-77.
663 [21] Gray LW, Peng F, Molloy SA, Pendyala VS, Muchenditsi A, Muzik O, Lee J, Kaplan JH, Lutsenko
664 S: Urinary copper elevation in a mouse model of Wilson's disease is a regulated process to specifically
665 decrease the hepatic copper load. PLoS One 2012, 7:e38327.
666 [22] Wooton-Kee CR, Robertson M, Zhou Y, Dong B, Sun Z, Kim KH, Liu H, Xu Y, Putluri N, Saha
667 P, Coarfa C, Moore DD, Nuotio-Antar AM: Metabolic dysregulation in the Atp7b(-/-) Wilson's disease
668 mouse model. Proc Natl Acad Sci U S A 2020, 117:2076-83.
669 [23] Sarode GV, Kim K, Kieffer DA, Shibata NM, Litwin T, Czlonkowska A, Medici V: Metabolomics
670 profiles of patients with Wilson disease reveal a distinct metabolic signature. Metabolomics 2019, 15:43.
671 [24] Yang Y, Schnabl B: Gut Bacteria in Alcohol-Associated Liver Disease. Clin Liver Dis 2024,
672 28:663-79.

673 [25] Leclercq S, Matamoros S, Cani PD, Neyrinck AM, Jamar F, Stärkel P, Windey K, Tremaroli V,
674 Bäckhed F, Verbeke K, de Timary P, Delzenne NM: Intestinal permeability, gut-bacterial dysbiosis, and
675 behavioral markers of alcohol-dependence severity. Proc Natl Acad Sci U S A 2014, 111:E4485-93.
676 [26] Soppert J, Brandt EF, Heussen NM, Barzakova E, Blank LM, Kuepfer L, Hornef MW, Trebicka J,
677 Jankowski J, Berres M-L: Blood endotoxin levels as biomarker of nonalcoholic fatty liver disease: a
678 systematic review and meta-analysis. Clinical Gastroenterology and Hepatology 2023, 21:2746-58.
679 [27] Martín-Mateos R, Albillos A: The Role of the Gut-Liver Axis in Metabolic Dysfunction-Associated
680 Fatty Liver Disease. Front Immunol 2021, 12:660179.
681 [28] Bergheim I, Moreno-Navarrete JM: The relevance of intestinal barrier dysfunction, antimicrobial
682 proteins and bacterial endotoxin in metabolic dysfunction-associated steatotic liver disease. Eur J Clin
683 Invest 2024, 54:e14224.
684 [29] Nishiwaki H, Ito M, Ishida T, Hamaguchi T, Maeda T, Kashihara K, Tsuboi Y, Ueyama J,
685 Shimamura T, Mori H, Kurokawa K, Katsuno M, Hirayama M, Ohno K: Meta-Analysis of Gut Dysbiosis
686 in Parkinson's Disease. Mov Disord 2020, 35:1626-35.
687 [30] Roberts EA, Robinson BH, Yang S: Mitochondrial structure and function in the untreated Jackson
688 toxic milk (tx-j) mouse, a model for Wilson disease. Mol Genet Metab 2008, 93:54-65.
689 [31] Hardie DG, Hawley SA, Scott JW: AMP-activated protein kinase--development of the energy
690 sensor concept. J Physiol 2006, 574:7-15.
691 [32] Liu Q, Liu LX, Li BM, Zhang W, Zhang Y, Chen P, Huang CK, Nie Y, Zhu X: Exploring the
692 mechanism of ursolic acid in preventing liver fibrosis and improving intestinal microbiota based on
693 NOX2/NLRP3 inflammasome signaling pathway. Chem Biol Interact 2025, 405:111305.
694 [33] Subramanian S, Geng H, Wu L, Du C, Peiper AM, Bu HF, Chou PM, Wang X, Tan SC, Iyer NR,
695 Khan NH, Zechner EL, Fox JG, Breinbauer R, Qi C, Yamini B, Ting JP, De Plaen IG, Karst SM, Tan
696 XD: Microbiota regulates neonatal disease tolerance to virus-evoked necrotizing enterocolitis by shaping
697 the STAT1-NLRC5 axis in the intestinal epithelium. Cell Host Microbe 2024, 32:1805-21.e10.

[34] Petruzzelli R, Catalano F, Crispino R, Polishchuk EV, Elia M, Masone A, Lavigna G, Grasso A, Battipaglia M, Sepe LV, Akdogan B, Reinold Q, Del Prete E, Carrella D, Torella A, Nigro V, Caruso E, Innocenti N, Biasini E, Puchkova LV, Indrieri A, Ilyechova EY, Piccolo P, Zischka H, Chiesa R, Polishchuk RS: Prion protein promotes copper toxicity in Wilson disease. Nat Commun 2025, 16:1468.

[35] Ralle M, Huster D, Vogt S, Schirrmeister W, Burkhead JL, Capps TR, Gray L, Lai B, Maryon E, Lutsenko S: Wilson disease at a single cell level: intracellular copper trafficking activates compartment-specific responses in hepatocytes. J Biol Chem 2010, 285:30875-83.

[36] Huster D, Purnat TD, Burkhead JL, Ralle M, Fiehn O, Stuckert F, Olson NE, Teupser D, Lutsenko S: High copper selectively alters lipid metabolism and cell cycle machinery in the mouse model of Wilson disease. J Biol Chem 2007, 282:8343-55.

[37] Zhang S, Chen S, Li W, Guo X, Zhao P, Xu J, Chen Y, Pan Q, Liu X, Zychlinski D, Lu H, Tortorella MD, Schambach A, Wang Y, Pei D, Esteban MA: Rescue of ATP7B function in hepatocyte-like cells from Wilson's disease induced pluripotent stem cells using gene therapy or the chaperone drug curcumin. Hum Mol Genet 2011, 20:3176-87.

[38] Overeem AW, Klappe K, Parisi S, Klöters-Planchy P, Mataković L, du Teil Espina M, Drouin CA, Weiss KH, van ISCD: Pluripotent stem cell-derived bile canaliculi-forming hepatocytes to study genetic liver diseases involving hepatocyte polarity. J Hepatol 2019, 71:344-56.

[39] Kim D, Kim SB, Ryu JL, Hong H, Chang JH, Yoo TJ, Jin X, Park HJ, Han C, Lee BH, Choi JH, Yoo HW, Kim JH, Woo DH: Human Embryonic Stem Cell-Derived Wilson's Disease Model for Screening Drug Efficacy. Cells 2020, 9.

[40] Wei R, Yang J, Cheng CW, Ho WI, Li N, Hu Y, Hong X, Fu J, Yang B, Liu Y, Jiang L, Lai WH, Au KW, Tsang WL, Tse YL, Ng KM, Esteban MA, Tse HF: CRISPR-targeted genome editing of human induced pluripotent stem cell-derived hepatocytes for the treatment of Wilson's disease. JHEP Rep 2022, 4:100389.

[41] Song D, Takahashi G, Zheng YW, Matsuo-Takasaki M, Li J, Takami M, An Y, Hemmi Y, Miharada N, Fujioka T, Noguchi M, Nakajima T, Saito MK, Nakamura Y, Oda T, Miyaoka Y, Hayashi Y: Retinoids rescue ceruloplasmin secretion and alleviate oxidative stress in Wilson's disease-specific hepatocytes. Hum Mol Genet 2022, 31:3652-71.

FIGURE LEGENDS

Figure 1. Copper quantification. Liver and IEC copper in male (A, B) and female (C, D) *Atp7b*$^{-/-}$ and *Atp7b*$^{\Delta IEC}$ mice at 9, 16, 24, and 30 weeks of age. Values are means ± SEM and statistical significance was determined by Student's t test. ** p<0.01, *** p<0.001, **** p<0.0001.
(n): Liver male *Atp7b*$^{-/-}$ 9w (4), 16 w (11), 24 w (3), 30 w (5); Liver male WT 9 w (5), 16 w (12), 24 w (5), 30 w (5); Liver male *Atp7b*$^{\Delta IEC}$ 9w (4), 16 w (10), 24 w (7), 30 w (6); Liver male iWT 9 w (4), 16 w (11), 24 w (7), 30 w (7); Liver female *Atp7b*$^{-/-}$ 9w (5), 16 w (6), 24 w (6), 30 w (4); Liver female WT 9 w (5), 16 w (5), 24 w (3), 30 w (5); Liver female *Atp7b*$^{\Delta IEC}$ 9w (3), 16 w (7), 24 w (7), 30 w (7); Liver female iWT 9 w (7), 16 w (7), 24 w (7), 30 w (7); IECs male *Atp7b*$^{-/-}$ 9w (1), 16 w (7), 24 w (4), 30 w (6); IECs male WT 9 w (2), 16 w (6), 24 w (5), 30 w (5); IECs male *Atp7b*$^{\Delta IEC}$ 9w (4), 16 w (7), 24 w (7), 30 w (5); IECs male iWT 9 w (5), 16 w (7), 24 w (7), 30 w (5); IECs female *Atp7b*$^{-/-}$ 16 w (7), 24 w (6); IECs female WT 16 w (7), 24 w (4); IECs female *Atp7b*$^{\Delta IEC}$ 9w (4), 16 w (7), 24 w (7), 30 w (6); IECs female iWT 9 w (4), 16 w (7), 24 w (7), 30 w (6).
✦ Due to the small sample size, 9-week *Atp7b*$^{-/-}$ and WT IEC copper are presented with sexes combined. *Atp7b*$^{-/-}$, *Atp7b* global knockout on C57Bl/6 background; *Atp7b*$^{\Delta IEC}$, intestine epithelial cell-specific knockout on C57Bl/6 background; iWT, wildtype controls (Lox$^{+/+}$:Cre^{-}) for *Atp7b*$^{\Delta IEC}$; WT, wildtype controls (*Atp7b*$^{+/+}$) for *Atp7b*$^{-/-}$.

Figure 2. Cholesterol and triglycerides. Plasma cholesterol (A, C), plasma triglycerides (B, D), liver cholesterol (E, G), and liver triglycerides (F, H) in *Atp7b*$^{-/-}$ and *Atp7b*$^{\Delta IEC}$ mice. Values are means ± SEM and statistical significance was determined by Student's t test. * p<0.05, ** p<0.01, *** p<0.001, **** p<0.0001. (n): Plasma male *Atp7b*$^{-/-}$ 9w (3), 16 w (11), 24 w (8), 30 w (10); Plasma male WT 9 w (3), 16 w (12), 24 w (11), 30 w (12); Plasma male *Atp7b*$^{\Delta IEC}$ 9w (4), 16 w (10), 24 w (12), 30 w (6); Plasma male iWT 9 w (4), 16 w (11), 24 w (11), 30 w (7); Plasma female *Atp7b*$^{-/-}$ 9 w (3), 16 w (11), 24 w (10), 30 w (13); Plasma female WT 9 w (3), 16 w (13), 24 w (10), 30 w (13) ; Plasma female *Atp7b*$^{\Delta IEC}$: 9 w (4), 16 w (14), 24 w (10), 30 w (9); Plasma female iWT 9 w (3), 16 w (12), 24 w (10), 30 w (9); Liver male *Atp7b*$^{-/-}$ 9w (3), 16 w (11), 24 w (8), 30 w (10); Liver male WT 9 w (3), 16 w (12), 24 w (10), 30 w (13); Liver male *Atp7b*$^{\Delta IEC}$ 9w (4), 16 w (10), 24 w (12), 30 w (6); Liver male iWT 9 w (4), 16 w (11), 24 w (11), 30 w (7); Liver female *Atp7b*$^{-/-}$ 9w (3), 16 w (11), 24 w (10), 30 w (13); Liver female WT 9 w (3), 16 w (12), 24 w (10), 30 w (13); Liver female *Atp7b*$^{\Delta IEC}$ 9w (4), 16 w (14), 24 w (10), 30 w (9); Liver female iWT 9 w (3), 16 w (12), 24 w (10), 30 w (9). *Atp7b*$^{-/-}$, *Atp7b* global knockout on C57Bl/6 background; *Atp7b*$^{\Delta IEC}$, intestine epithelial cell-specific knockout on C57Bl/6 background; iWT, wildtype controls (Lox$^{+/+}$:Cre^{-}) for *Atp7b*$^{\Delta IEC}$; WT, wildtype controls (*Atp7b*$^{+/+}$) for *Atp7b*$^{-/-}$.

Figure 3. *Atp7b*$^{-/-}$ liver histology. Representative H&E liver sections from *Atp7b*$^{-/-}$ mice and WT controls at 9 (A, B), 16 (C, D), 24 (E, F), and 30 (G, H) weeks of age. Liver histology is normal in WT control mice. *Atp7b*$^{-/-}$ mouse livers present progressively enlarged hepatocytes with enlarged and glycogenated hepatocyte nuclei as well as both portal and lobular lymphocytic infiltrates. Scale bar = 300μm at 10X magnification. (n): *Atp7b*$^{-/-}$ 9 w (9), 16 w (27), 24 w (21), 30 w (23); WT 9 w (9), 16 w (30), 24 w (25), 30 w (25). *Atp7b*$^{-/-}$, *Atp7b* global knockout on C57Bl/6 background; WT, wildtype controls (*Atp7b*$^{+/+}$) for *Atp7b*$^{-/-}$.

Figure 4. *Atp7b*$^{\Delta IEC}$ liver histology. Representative H&E liver sections from *Atp7b*$^{\Delta IEC}$ mice and iWT controls at 9 (A, B), 16 (C, D), 24 (E, F), and 30 (G, H) weeks of age. Liver histology in iWT control mice and *Atp7b* $^{\Delta IEC}$ mouse livers is similar with development of mild glycogenosis over time. Scale bar = 300 μm at 10X magnification. (n): *Atp7b*$^{\Delta IEC}$ 9w (8), 16 w (28), 24 w (28), 30 w (21); iWT 9 w

(7), 16 w (27), 24 w (27), 30 w (22). *Atp7b*$^{\Delta IEC}$, intestine epithelial cell-specific knockout on C57Bl/6 background; iWT, wildtype controls (Lox$^{+/+}$:Cre^{-}) for *Atp7b*$^{\Delta IEC}$.

Figure 5. Intestine histology. Representative small intestine H&E from *Atp7b*$^{-/-}$ and *Atp7b*$^{\Delta IEC}$ mice. At 16 and 24 weeks of age, intestine histology in *Atp7b*$^{-/-}$ (B, D) and *Atp7b*$^{\Delta IEC}$ (F, H) mice appears similar to their respective controls, WT (A, C) and iWT (E, G). Scale bar = 300 μm at 10X magnification. (n): *Atp7b*$^{-/-}$ 16 w (4), 24 w (4); WT 16 w (1), 24 w (1); *Atp7b*$^{\Delta IEC}$ 16 w (8), 24 w (11); iWT 16 w (4), 24 w (8). *Atp7b*$^{-/-}$, *Atp7b* global knockout on C57Bl/6 background; *Atp7b*$^{\Delta IEC}$, intestine epithelial cell-specific knockout on C57Bl/6 background; iWT, wildtype controls (Lox$^{+/+}$:Cre^{-}) for *Atp7b*$^{\Delta IEC}$; WT, wildtype controls (*Atp7b*$^{+/+}$) for *Atp7b*$^{-/-}$.

Figure 6. Mitochondrial alterations in *Atp7b*$^{-/-}$ and *Atp7b*$^{\Delta IEC}$ mouse IECs. Transmission electron microscopy of normal mitochondria in WT and iWT intestine with electron dense matrices and organized cristae (A, B). *Atp7b*$^{-/-}$ and *Atp7b*$^{\Delta IEC}$ mice frequently exhibit several mitochondrial abnormalities such as unorganized and depleted cristae, distorted inner and outer membrane, ballooning, and electro-lucent matrices (C, D, E, F). *Atp7b*$^{\Delta IEC}$ also display a significant number of mitochondria with dilated cristae (C, D, E, H, white arrows). Occasionally, mitochondria with U-shaped morphology also appear (G, H). (n): WT=2; *Atp7b*$^{-/-}$=4; iWT=2; *Atp7b*$^{\Delta IEC}$=8; 30-40 images per n. Scalebar = 500 nm or 1 μm, as noted. All panels = 16 weeks, except panel E = 24 weeks. *Atp7b*$^{-/-}$, *Atp7b* global knockout on C57Bl/6 background; *Atp7b*$^{\Delta IEC}$, intestine epithelial cell-specific knockout on C57Bl/6 background; iWT, wildtype controls (Lox$^{+/+}$:Cre^{-}) for *Atp7b*$^{\Delta IEC}$; WT, wildtype controls (*Atp7b*$^{+/+}$) for *Atp7b*$^{-/-}$.

Figure 7. Alterations in the *Atp7b*$^{-/-}$ and *Atp7b*$^{\Delta IEC}$ mouse IEC barrier. Transmission electron microscopy of normal junctional complexes at the apical surface in WT and iWT IECs (A, B). *Atp7b*$^{-/-}$ and *Atp7b*$^{\Delta IEC}$ IECs frequently exhibit alterations to parts of the junctional complex and lateral membranes. One-sided desmosomes at the junctional complex (C, D, circled) and elsewhere along the lateral membranes are common occurrences in both strains. The gap at the adherens junction and desmosomes are also often abnormally wide (E, F). *Atp7b*$^{-/-}$ IECs, in particular, form lateral membranes that loop back and forth excessively (G) compared to controls and *Atp7b*$^{\Delta IEC}$ IECs (H). (n): WT=2; *Atp7b*$^{-/-}$=4; iWT=2; *Atp7b*$^{\Delta IEC}$=8; 30-40 images per n. Scalebar = 500 nm. Panels A, C, E = 16 weeks, panels B, D, F, G, H = 24 weeks. AJ; adherens junction; *Atp7b*$^{-/-}$, *Atp7b* global knockout on C57Bl/6 background; *Atp7b*$^{\Delta IEC}$, intestine epithelial cell-specific knockout on C57Bl/6 background; Des, desmosome; iWT, wildtype controls (Lox$^{+/+}$:Cre^{-}) for *Atp7b*$^{\Delta IEC}$; TJ, tight junction; WT, wildtype controls (*Atp7b*$^{+/+}$) for *Atp7b*$^{-/-}$.

Figure 8. Hepatic AMPK signaling heat map in *Atp7b*$^{-/-}$ mice at 16 weeks of age. Hierarchical heat map clustering of samples based on Pearson's correlation coefficient for genes in the AMPK signaling pathway determined by KEGG Pathway Analysis in the livers of *Atp7b*$^{-/-}$ at 16 weeks of age. (n): *Atp7b*$^{-/-}$ (6), WT (6). *Atp7b*$^{-/-}$, *Atp7b* null global knockout on C57Bl/6 background; WT, wildtype controls (*Atp7b*$^{+/+}$) for *Atp7b*$^{-/-}$.

Figure 9. Hepatic AMPK signaling at 16 weeks of age in *Atp7b*$^{-/-}$ and *Atp7b*$^{\Delta IEC}$ mice. Hierarchical heat map (A) clustering of samples based on Pearson's correlation coefficient for genes in the AMPK signaling pathway determined by KEGG Pathway Analysis in the livers of *Atp7b*$^{\Delta IEC}$ mice at 16 weeks of age. Relative expression of genes for both *Atp7b*$^{-/-}$ and *Atp7b*$^{\Delta IEC}$ mice in the AMPK signaling pathway — Stearoyl-CoA desaturase 3 (*Scd3*) (B), Lipase E (*Lipe)* (C), and acyl-CoA synthase long chain family member 3 (*Acsl3*) (D). Values are means ± SEM and statistical significance was determined by Student's t test. * $p<0.05$, *** $p<0.001$. (n): *Atp7b*$^{-/-}$ (6), WT (6), *Atp7b*$^{\Delta IEC}$ (6), iWT (6).

862 *Atp7b*$^{-/-}$, *Atp7b* null global knockout on C57Bl/6 background; *Atp7b*$^{\Delta IEC}$, intestine epithelial cell-
863 specific knockout on C57Bl/6 background; iWT, wildtype controls (Lox$^{+/+}$:Cre^{-}) for *Atp7b*$^{\Delta IEC}$; WT,
864 wildtype controls (*Atp7b*$^{+/+}$) for *Atp7b*$^{-/-}$.
865
866 **Figure 10. Hepatic AMPK signaling heat map in *Atp7b*$^{-/-}$ mice at 30 weeks of age.** Hierarchical heat
867 map clustering of samples based on Pearson's correlation coefficient for genes in the AMPK signaling
868 pathway determined by KEGG Pathway Analysis in the livers of *Atp7b*$^{-/-}$ mice at 30 weeks of age. (n):
869 *Atp7b*-/- (6), WT (6). *Atp7b*$^{-/-}$, *Atp7b* null global knockout on C57Bl/6 background; WT, wildtype
870 controls (*Atp7b*$^{+/+}$) for *Atp7b*$^{-/-}$.
871
872 **Figure 11. Hepatic AMPK signaling at 30 weeks of age in *Atp7b*$^{-/-}$ and *Atp7b*$^{\Delta IEC}$ mice.** Hierarchical
873 heat map clustering of samples based on Pearson's correlation coefficient for genes in the AMPK
874 signaling pathway determined by KEGG Pathway Analysis in the livers of *Atp7b*$^{-/-}$ (A) and *Atp7b*$^{\Delta IEC}$
875 (B) mice at 30 weeks of age. Relative expression (B) of sterol regulatory element binding transcription
876 factor 1 (*Srebf1*) for both *Atp7b*$^{-/-}$ and *Atp7b*$^{\Delta IEC}$ mice. Values are means ± SEM and statistical
877 significance was determined by Student's t test. * $p<0.05$, *** $p<0.001$. (n): *Atp7b*-/- (6), WT (6),
878 *Atp7b*$^{\Delta IEC}$ (6), iWT (6). *Atp7b*$^{-/-}$, *Atp7b* null global knockout on C57Bl/6 background; *Atp7b*$^{\Delta IEC}$,
879 intestine epithelial cell-specific knockout on C57Bl/6 background; iWT, wildtype controls (Lox$^{+/+}$:Cre^{-}
880) for *Atp7b*$^{\Delta IEC}$; WT, wildtype controls (*Atp7b*$^{+/+}$) for *Atp7b*$^{-/-}$.
881
882
883
884
885
886
887
888
889
890
891
892
893
894
895

Table 1. Body weights and normalized liver weights.

9 weeks						
Genotype	n		Body Weight (g)		Liver / Body Weight	
	M	F	Male	Female	Male	Female
WT	5	4	23.9 ± 1.6	20.4 ± 0.5†††	0.056 ± 0.002	0.049 ± 0.010
Atp7b$^{-/-}$	4	5	24.3 ± 1.8	20.2 ± 1.6†††	0.053 ± 0.002	0.050 ± 0.007
iWT	4	3	28.0 ± 0.4	20.2 ± 1.1†††	0.046 ± 0.003	0.053 ± 0.003
Atp7b$^{\Delta IEC}$	4	4	23.9 ± 1.4**	19.8 ± 0.1†††	0.055 ± 0.007*	0.057 ± 0.004
16 weeks						
Genotype	n		Body Weight (g)		Liver / Body Weight	
	M	F	Male	Female	Male	Female
WT	12	13	29.2 ± 1.8	23.6 ± 1.7†††	0.049 ± 0.006	0.045 ± 0.007
Atp7b$^{-/-}$	10	11	27.7 ± 1.7	23.0 ± 1.1†††	0.053 ± 0.003	0.056 ± 0.011*
iWT	11	12	29.5 ± 1.7	22.8 ± 1.3†††	0.050 ± 0.005	0.048 ± 0.004
Atp7b$^{\Delta IEC}$	10	14	28.5 ± 1.9	22.7 ± 1.1†††	0.048 ± 0.004	0.049 ± 0.004
24 weeks						
Genotype	n		Body Weight (g)		Liver / Body Weight	
	M	F	Male	Female	Male	Female
WT	12	10	29.6 ± 2.5	24.3 ± 2.2†††	0.049 ± 0.005	0.046 ± 0.007
Atp7b$^{-/-}$	12	9	28.1 ± 2.1	23.7 ± 0.8†††	0.062 ± 0.007**	0.062 ± 0.017*
iWT	11	10	32.0 ± 2.4	23.7 ± 1.5†††	0.048 ± 0.005	0.043 ± 0.005††
Atp7b$^{\Delta IEC}$	12	10	31.8 ± 1.6	23.5 ± 0.8†††	0.048 ± 0.004	0.048 ± 0.010
30 weeks						
Genotype	n		Body Weight (g)		Liver / Body Weight	
	M	F	Male	Female	Male	Female
WT	12	13	32.1 ± 2.5	25.4 ± 1.8†††	0.045 ± 0.006	0.046 ± 0.005
Atp7b$^{-/-}$	10	14	27.2 ± 2.0***	22.8 ± 1.5†††***	0.064 ± 0.009***	0.066 ± 0.011***
iWT	11	11	32.6 ± 2.8	26.1 ± 2.3†††	0.045 ± 0.005	0.004 ± 0.005
Atp7b$^{\Delta IEC}$	10	11	32.9 ± 2.0	25.9 ± 2.6†††	0.044 ± 0.005	0.004 ± 0.004

Values are mean ± SD and statistical significance was determined by Student's t test. An asterisk (*) indicates values are significantly different between a WD model (*Atp7b*$^{-/-}$ or *Atp7b*$^{\Delta IEC}$) and its respective control (WT or iWT) within the same sex (* $p<0.05$, ** $p<0.01$, *** $p<0.001$). A dagger (†) indicates values are significantly different between sexes within the same genotype (†† $p<0.01$, ††† $p<0.001$).

Atp7b$^{-/-}$, *Atp7b* null global knockout on C57Bl/6 background; *Atp7b*$^{\Delta IEC}$, intestine epithelial cell-specific knockout on C57Bl/6 background; iWT, wildtype controls (Lox$^{+/+}$:Cre^{-}) for *Atp7b*$^{\Delta IEC}$; WT, wildtype controls (*Atp7b*$^{+/+}$) for *Atp7b*$^{-/-}$.

Table 2. Alanine Transaminase and ceruloplasmin activity levels.

Genotype	n		Alanine Transaminase (U/L)		n		Ceruloplasmin activity (mU/ml)	
	M	F	Male	Female	M	F	Male	Female
9 weeks								
WT	5	4	40.2 ± 22.7	31.9 ± 10.9				
Atp7b$^{-/-}$	4	5	28.5 ± 5.0	35.1 ± 14.9				
iWT	4	3	41.3 ± 5.4	30.6 ± 9.2				
Atp7b$^{\Delta IEC}$	4	4	31.4 ± 9.4	29.7 ± 11.3				
16 weeks								
WT	12	13	80.2 ± 69.7	68.2 ± 60.8	4	4	8256 ± 1406	9500 ± 2418
Atp7b$^{-/-}$	10	11	216.0 ± 83.7*	164.6 ± 51.2*	4	4	9658 ± 2353	6342 ± 1660*
iWT	11	12	67.9 ± 36.7	95.7 ± 44.2	4	4	9593 ± 2864	10059 ± 1689
Atp7b$^{\Delta IEC}$	10	14	63.3 ± 11.0	46.9 ± 26.8	4	4	8795 ± 2471	10242 ± 3075
24 weeks								
WT	12	10	131.0 ± 51.3	50.8 ± 19.9†				
Atp7b$^{-/-}$	12	9	348.9 ± 139.4*	268.5 ± 147.7*				
iWT	11	10	83.9 ± 34.2	58.9 ± 44.4				
Atp7b$^{\Delta IEC}$	12	10	106.5 ± 44.0	68.5 ± 37.9				
30 weeks								
WT	12	13	62.6 ± 25.3	80.3 ± 18.0	4	4	9307 ± 3230	10035 ± 2902
Atp7b$^{-/-}$	10	14	421.4 ± 93.9**	363.4 ± 126.9**	4	4	9356 ± 2963	11450 ± 980
iWT	11	11	43.1 ± 24.1	29.2 ± 7.9	4	4	8584 ± 1955	7721 ± 2148
Atp7b$^{\Delta IEC}$	10	11	58.6 ± 49.8	29.5 ± 4.5	4	4	9848 ± 3515	9644 ± 2512

Values are mean ± SD and statistical significance was determined by Student's t test. An asterisk (*) indicates values are significantly different between a WD model (*Atp7b*$^{-/-}$ or *Atp7b*$^{\Delta IEC}$) and its respective control (WT or iWT) within the same sex (* $p<0.05$, ** $p<0.01$). A dagger (†) indicates values are significantly different between sexes within the same genotype († $p<0.05$).
Atp7b$^{-/-}$, *Atp7b* global knockout on C57Bl/6 background; *Atp7b*$^{\Delta IEC}$, intestine epithelial cell-specific knockout on C57Bl/6 background; iWT, wildtype controls (Lox$^{+/+}$:Cre^{-}) for *Atp7b*$^{\Delta IEC}$; WT, wildtype controls (*Atp7b*$^{+/+}$) for *Atp7b*$^{-/-}$.